

Lawrence Berkeley National Laboratory

Recent Work

Title

Trace doping of multiple elements enables stable battery cycling of LiCoO₂ at 4.6 V

Permalink

<https://escholarship.org/uc/item/2vp9t743>

Journal

Nature Energy, 4(7)

ISSN

2058-7546

Authors

Zhang, JN

Li, Q

Ouyang, C

et al.

Publication Date

2019-07-01

DOI

10.1038/s41560-019-0409-z

Peer reviewed

1 **Trace doping of multiple elements enables stable battery cycling of**

2 **LiCoO₂ at 4.6 V**

3 Jie-Nan Zhang^{1,2†}, Qinghao Li^{1,3†}, Chuying Ouyang⁴, Xiqian Yu^{1,2*}, Mingyuan Ge⁵,
4 Xiaojing Huang⁵, Enyuan Hu⁵, Chao Ma⁶, Shaofeng Li⁷, Ruijuan Xiao¹, Wanli Yang³,
5 Yong Chu⁵, Yijin Liu^{7*}, Huigen Yu⁸, Xiao-Qing Yang⁵, Xuejie Huang¹, Liquan Chen¹,
6 Hong Li^{1,2*}

7 1 Beijing Advanced Innovation Center for Materials Genome Engineering, Institute of
8 Physics, Chinese Academy of Sciences, Beijing 100190, China.

9 2 Center of Materials Science and Optoelectronics Engineering, College of Materials
10 Science and Opto-Electronic Technology, University of Chinese Academy of
11 Sciences, Beijing 100049, China.

12 3 Advanced Light Source, Lawrence Berkeley National Laboratory, Berkeley, CA
13 94720, USA.

14 4 Department of Physics, Laboratory of Computational Materials Physics, Jiangxi
15 Normal University, Jiangxi 330022, China.

16 5 Brookhaven National Laboratory, Upton, NY 11973, USA.

17 6 College of Materials Science and Engineering, Hunan University, Changsha 410082,
18 China.

19 7 Stanford Synchrotron Radiation Lightsource, SLAC National Accelerator
20 Laboratory, Menlo Park, CA 94025, USA.

21 8 Beijing WeLion New Energy Technology Co., Ltd., Beijing 102402, China.

22

23 Corresponding authors: X.Y. (xyu@iphy.ac.cn), Y.L. (liyijin@slac.stanford.edu) and
24 H.L. (hli@iphy.ac.cn)

25 **LiCoO₂ is a dominant cathode material for Li-ion batteries due to its high**
26 **volumetric energy density, which could potentially be further improved by**
27 **charging to high voltage. Practical adoption of the high-voltage charging is,**
28 **however, hindered by LiCoO₂'s structural instability at the deeply delithiated**
29 **state and the associated safety concerns. Here, we achieve stable cycling of**
30 **LiCoO₂ at 4.6 V (vs. Li/Li⁺) through trace Ti-Mg-Al co-doping. By using**
31 **state-of-the-art synchrotron X-ray imaging and spectroscopic techniques, we**
32 **confirm the incorporation of Mg and Al into the LiCoO₂ lattice, which inhibits**
33 **the undesired phase transition at voltages above 4.5 V. On the other hand, even**
34 **in trace amount, Ti segregates significantly at grain boundaries and on the**
35 **surface, modifying the microstructure of the particles while stabilizing the**
36 **surface oxygen at high voltage. These dopants contribute through different**
37 **mechanisms and synergistically promote the cycle stability of LiCoO₂ at 4.6 V.**

38

39 The constantly increasing energy consumption of modern society has led to the
40 demand for energy storage technology with higher energy densities^{1,2,3}. Li-ion
41 batteries (LIBs) are the most popular energy storage devices, which are widely
42 deployed in portable electronics and, more recently, in electric vehicles. The energy
43 density of LIBs is directly proportional to the working voltage and the lithium storage
44 capacity. Therefore, the development of cathode materials that are of larger reversible
45 capacity and are compatible with higher voltage charging has been a hot research
46 topic^{4,5,6,7}. Thanks to the tremendous research efforts devoted over the past few
47 decades, we have witnessed the successful commercialization of quite a number of
48 cathode materials (see the comparison of their theoretical energy densities in
49 Supplementary Fig. 1). We note here that LiCoO₂, which was first recognised as a
50 cathode material with good potential in the 1980s, still presents competitive or even
51 superior energy density among all the cathode materials that are commercially
52 available. As a key player on today's market of cathode materials, LiCoO₂ exhibits
53 many essential advantages, including high theoretical capacity, high Li⁺/electron
54 conductivity, high theoretical density and high compressed density for electrode^{8,9,10}.
55 While the theoretical capacity of LiCoO₂ is as high as 274 mAh g⁻¹, its practical
56 discharge capacity with acceptable level of cycle reversibility is only about 173 mAh
57 g⁻¹ (Li_{1-x}CoO₂, x≈0.63, 4.45 V vs. Li/Li⁺). Increasing the charging cut-off voltage to
58 extract more Li⁺ can further increase the capacity of LiCoO₂ (e.g. 4.5 V vs. Li/Li⁺,
59 6.9% increase in capacity, ~185 mAh g⁻¹; 4.6 V vs. Li/Li⁺, 27.2% increase in capacity,
60 ~220 mAh g⁻¹), however, such practice could lead to several detrimental problems,

61 causing rapid decay of cycle efficiency and capacity. More specifically, when the
62 voltage reaches 4.5 V, a harmful phase transformation from O3 hexagonal phase to
63 hybridized O1-O3 hexagonal phase (denoted as H1-3 phase. O: octahedral sites; 3:
64 stacking sequence of oxygen layers ABCABC and 1: ABAB) occurs and is
65 accompanied with gliding of lattice slabs and partial collapse of the O3 lattice
66 structure¹¹. Consequently, the internal strain builds up, leading to crack formation and
67 particle pulverization^{11,12}. Meanwhile, oxygen loss at high voltage further brings
68 irreversible phase transition or even safety concerns. Besides these structural failure
69 modes in the bulk, the surface instability is another critical issue that is amplified at
70 the high state of charge. The high valence Co/O could trigger undesired interfacial
71 side reactions, involving the oxidization of the electrolyte. All these factors add up to
72 serious performance degradation of LiCoO₂ at high voltage, jeopardizing the practical
73 application of the significantly increased capacity^{13,14,15,16}.

74

75 Many strategies have been considered to promote the cycle stability of LiCoO₂ at
76 high voltage^{17,18,19,20,21}. Among various approaches, foreign element doping is the
77 most prevailing and has been demonstrated to be promising and effective for the
78 improvement of the electrochemical performances of LiCoO₂^{22,23,24,25}. For example, a
79 study compared the cycle performances of doped LiCoO₂ at a high charging voltage
80 of 4.5 V with various transition metal ions (LiTM_{0.05}Co_{0.95}O₂, TM=Mn, Fe, Cu and
81 Zn)²⁶, and found that Mn doping enhanced reversible capacity the most to ~158 mAh
82 g⁻¹, in comparison with ~138 mAh g⁻¹ of bare LiCoO₂ after 50 cycles in the voltage

83 range of 3.5-4.5 V. It is also reported that concurrent doping of La, Al can greatly
84 improve the Li diffusivity and structure stability of LiCoO_2 ¹⁶. With such doping
85 strategy, LiCoO_2 can achieve high capacity of 190 mAh g^{-1} over 50 cycles at high
86 cut-off voltage of 4.5 V. We point out here that, while these previous works
87 instinctively assume that the dopants are well incorporated into parent lattice,
88 theoretical calculations have predicted the limited solubility of foreign atoms in
89 LiCoO_2 in some cases²⁷. Such inconsistencies necessitate in-depth investigations of
90 the fundamental roles of various dopants in improving the battery performances.
91 Compared with the literature reports based on laboratory-scale experiments, it is
92 worth noting that the doping concentration is generally 2-3 orders of magnitude lower
93 for industrial production. Therefore, for LiCoO_2 with low concentration doping at a
94 level of industrial relevance, empirical accumulation is of vital significance and the
95 corresponding fundamental research is urgently needed. Moreover, multiple-elements
96 co-doping is commonly executed in practice. The desired synergistic effect among
97 multiple dopants needs further exploration, but the characterisations of multiple
98 doping elements at low concentrations are daunting challenging.

99

100 In this work, we show that trace amount of Ti-Mg-Al co-doping ($\sim 0.1 \text{ wt}\%$ for each
101 dopant) can greatly improve the cycle and rate performances of LiCoO_2 at a high
102 charging cut-off voltage of 4.6 V. The fundamental roles of each individual dopant in
103 promoting the electrochemical performances are systematically studied by combining
104 various characterisations techniques including synchrotron X-ray spectroscopy and

105 X-ray imaging. We find that Al, Mg atoms are successfully incorporated into the
106 LiCoO_2 lattice and can effectively suppress the detrimental phase transition at high
107 charging voltage (above 4.5 V). However, even at trace amount, Ti segregates at grain
108 boundaries and on particle surface, facilitating fast lithium diffusion and alleviating
109 internal strain within the assembled LiCoO_2 particle. Moreover, the Ti-rich surface
110 can stabilize the oxygen redox and inhibit the undesired electrode-electrolyte
111 interfacial reactions. These experimental findings are further explained by first
112 principles calculations, demonstrating that the extraordinary battery performances of
113 Ti-Mg-Al co-doped LiCoO_2 can be attributed to both microstructure changes and
114 electronic structure reconfiguration induced by trace amount co-doping of Ti, Mg and
115 Al.

116

117 **Characterisations of Bare-LCO and TMA-LCO**

118 Undoped LiCoO_2 (Bare-LCO), Ti, Mg, Al single-element-doped LiCoO_2 and
119 Ti-Mg-Al co-doped LiCoO_2 (TMA-LCO) were prepared using a solid-state reaction
120 method. The inductively coupled plasma (ICP) emission spectroscopy results in
121 Supplementary Table 1 indicate that the actual chemical compositions of these
122 as-synthesised materials agree well with the intended compositions. Diverse
123 characterisations of the synthesised materials were performed and the results are
124 summarised in Supplementary Tables 2-4 and Supplementary Figs. 2-4. It is evident
125 that foreign-atom doping has a significant influence on various aspects of the physical
126 properties of LiCoO_2 , such as structural parameters, particle size, morphology and

127 conductivity. The doping elements, especially Ti, can introduce lattice strain and
128 slightly reduce the particle size of LiCoO₂. Moreover, Mg doping causes an increase
129 in electronic conductivity, whereas Al doping has minimal impact on these physical
130 parameters.

131

132 Here, we focus on TMA-LCO, which shows the best electrochemical performances.
133 The Rietveld refinements of XRD patterns of Bare-LCO and TMA-LCO indicate a
134 pure *R-3 m* layered structure with negligible differences in lattice parameters
135 (Supplementary Fig. 2 and Supplementary Table 4). As shown in Figs. 1a and 1b, the
136 primary particle size of TMA-LCO (D50: ~15 μm) is slightly smaller than that of
137 Bare-LCO (D50: ~16 μm). Further elemental mappings of the local region over a
138 TMA-LCO particle demonstrate an overall homogeneous distribution of the foreign
139 elements Ti, Mg and Al (Fig. 1d) except for the Ti-rich edge region. In view of the
140 resolution limit of elemental mapping, energy-dispersive X-ray spectroscopy (EDS)
141 and electron energy loss spectroscopy (EELS) measurements were carried out,
142 revealing the slight differences in elemental concentration between the centre and
143 edge areas of TMA-LCO particle. As highlighted in Figs. 1e and 1f, both EDS and
144 EELS results show that Ti has a higher elemental concentration at the surface than in
145 the interior of the particle but there is no evident difference for Mg and Al. To further
146 confirm this phenomenon, elemental distribution near the particle edge in a finer area
147 was analyzed. The high-angle annular dark-field (HAADF) image and elemental
148 mappings near the particle edge of the cross-sectional TEM sample are shown in

149 Supplementary Fig. 5, which demonstrate Ti aggregation at particle surface. X-ray
150 photoelectron spectroscopy (XPS) etching results further confirm the heterogeneity of
151 the spatial distribution of Ti within the particles (Supplementary Fig. 6).

152

153 **Electrochemical performances**

154 The electrochemical performances of Bare-LCO and TMA-LCO were evaluated in
155 both half-cells and full-cells, and the results are displayed in Figs. 2a-2e and
156 Supplementary Figs. 7 and 8 (initial charge-discharge curves and cycle/rate
157 performances respectively). It is apparent that TMA-LCO presents improved cycle
158 stability in half-cell compared with Bare-LCO, in particular at high charging cut-off
159 voltage of 4.6 V. A high reversible discharge capacity of 174 mAh g^{-1} , with capacity
160 retention of 86% (compared with the 2nd cycle), is achieved in TMA-LCO after 100
161 cycles at a current rate of 0.5C ($1\text{C} = 274 \text{ mA g}^{-1}$, note that all cells were cycled at
162 0.1C for formation process at the 1st cycle). The Coulombic efficiency (CE) was also
163 recorded during electrochemical cycling. The TMA-LCO cell shows slightly higher
164 CE (93.7%) than Bare-LCO cell (90.2%) at 4.6 V charging for the 1st cycle, and
165 quickly increases to 99% after 3 cycles and remains stable for the subsequent cycles
166 (Supplementary Fig. 9). The charge-discharge profiles at selected cycle numbers are
167 presented in Figs. 2b and 2c. It can be seen that Bare-LCO has significantly degraded
168 voltage profiles after 50 cycles, indicating the severer structural degradation in
169 Bare-LCO than TMA-LCO. The cycle and rate performances of single-element-doped
170 LiCoO_2 were also evaluated and the results are shown in Supplementary Fig. 8. They

171 all show better cycle and rate performances than Bare-LCO but inferior to
172 TMA-LCO.

173

174 For potential practical applications, full pouch cells (~2.8 Ah) with Bare-LCO or
175 TMA-LCO cathodes and commercial graphite anodes were assembled and cycled at
176 room temperature in the voltage range of 3.0-4.55 V (equivalent to 4.6 V vs. Li/Li⁺).
177 As shown in Fig. 2d, the capacity of Bare-LCO fades quickly to 51.3 mAh g⁻¹ after 70
178 cycles. In contrast, the TMA-LCO cell shows much improved capacity retention with
179 a capacity of 178.2 mAh g⁻¹ after 70 cycles and much more stable CE than that of
180 Bare-LCO (Supplementary Fig. 10). The discharge voltage remains almost unchanged
181 at around 3.90 V for TMA-LCO, while it gradually drops to 3.51 V for Bare-LCO.
182 The seriously degraded cycle performance of Bare-LCO full-cell can be attributed to
183 the irreversible structural transformation and unwanted side reactions, which can be
184 further proved by the obvious gas generation in cycled pouch cell as shown in inset of
185 Fig. 2e. Overall, TMA-LCO shows much improved electrochemical performances in
186 both half-cell and full-cell at a high charging cut-off voltage of 4.6 V (vs. Li/Li⁺)
187 compared with Bare-LCO (comparison of the performances with literature reports for
188 high voltage LiCoO₂ are summarized in Supplementary Tables 5-6).

189

190 **Structural evolution during 1st charge-discharge process**

191 As the cycle stability of LiCoO₂ is strongly associated with its structural evolution,
192 *in situ* XRD experiments were performed to study the phase transition behaviour.

193 Although pristine Bare-LCO and TMA-LCO share a similar crystal structure, distinct
194 differences in structural evolution over the first charge-discharge process can be
195 observed as shown in Figs. 3a and 3b. The (003) and (107) diffraction peaks are
196 selected for demonstration. A relatively small (003) peak shift is observed in
197 TMA-LCO at high voltage 4.6 V, in contrast to the dramatic (003) peak shift in
198 Bare-LCO. This could be attributed to the suppressed O3 to H1-3 phase transition
199 which is accompanied with the oxygen stacking sequence change (Fig. 3d)^{28, 29}. Such
200 mitigation of structural changes is also demonstrated in the (107) peak shift as
201 highlighted by the vertical dotted lines in Figs. 3a and 3b. The (107) peak splitting at
202 4.1 V occurs in both Bare-LCO and TMA-LCO, which can be attributed to an
203 order-disorder transition^{30, 31}. Considering the superior battery performances of
204 TMA-LCO, the conversion between the hexagonal and monoclinic phases at around
205 4.1 V may not be the main cause for performance degradation. The phase transition
206 behaviour also manifests itself in the charge-discharge voltage profiles and cyclic
207 voltammetry (CV) curves of Bare-LCO and TMA-LCO, which are shown in Fig. 3c.
208 The persistence of the anodic and cathodic peaks due to the order-disorder transition
209 and the difference between Bare-LCO and TMA-LCO at a high voltage of 4.6 V are
210 consistent with the *in situ* XRD results.

211

212 **3D elemental distributions in TMA-LCO particle**

213 Considering the indication of a non-uniform dopant distribution from the EDS and
214 EELS results, it is necessary to determine the actual spatial distribution of the key

215 elements in the LiCoO_2 particles. X-ray fluorescence mapping, which is capable of
216 detecting the spatial elemental distribution and concentration with high sensitivity,
217 was utilised to probe the 3D elemental distribution within an arbitrarily selected
218 TMA-LCO particle. Because Mg was outside of the working energy window, only Al,
219 Co and Ti signals were collected and the 3D renderings of their distributions are
220 displayed in Figs. 4a-4c. Figs. 4d-4f show the elemental distributions over a virtual
221 x-z slice through the centre of the particle. The absolute concentrations of these
222 elements are very different as indicated by the coloured scale bar in the corresponding
223 insets. It is evident from Figs. 4a and 4d that Al is homogeneously distributed
224 throughout the entire particle with a minor degree of concentration variation. The Ti
225 distribution presented in Figs. 4c and 4f, on the other hand, shows a large degree of
226 segregation. The Ti-rich phase forms a complex interconnected network (as
227 highlighted by the dashed lines in Fig. 4f), dividing the LiCoO_2 particle into several
228 subdomains. For further evaluation of the subdomain separation effect, we first
229 calculated the Ti to Co ratio voxel by voxel throughout the entire 3D volume. Areas
230 with Ti: Co ratio equal to or below the nominal value are segmented as active
231 subdomains. As shown in Fig. 4g, a total number of 50 subdomains were identified
232 and visualised. Note that different colours are used to distinguish adjacent subdomains
233 for visualisation. However, colours are reused for subdomains that are far apart due to
234 the large number of subdomains identified. Further quantification of these
235 subdomains suggests that they have a wide distribution in volume and surface area, as
236 indicated by Figs. 4h and 4i. Compared with the entire particle as a whole, the

237 subdomains with largely reduced size and significantly increased surface area ensure
238 fast Li^+ diffusion in the micro-sized particles, which could be one major factor
239 responsible for the improved rate performance of TMA-LCO. In addition, the
240 subdomains separated by the Ti-rich phase can effectively reduce the lattice breathing
241 induced by Li intercalation and are more robust against lattice strain and particle
242 fracture, thereby possibly enhancing the long-term cycle stability of TMA-LCO. To
243 ensure the representativeness of the conclusion drawn from the single particle analysis,
244 we conducted two-dimensional (2D) elemental mapping over many TMA-LCO
245 particles using synchrotron based micro-probe. The correlation evaluation and the
246 principle component analysis (PCA) of the Co and Ti maps further confirm the
247 heterogeneity distribution of Ti from a statistical point of view (Supplementary Fig.
248 11).

249

250 **Surface reaction probed by soft X-ray spectroscopy**

251 Soft X-ray spectroscopy measurements were performed to study the surface
252 properties of Bare-LCO and TMA-LCO³². Considering the strong correlation between
253 oxygen involvement and battery failure at high voltage, the O-*K* edge spectra are the
254 research focus. Note that the strong hybridisation between TM *3d* and O *2p* states
255 makes it challenging to separate out the lattice oxygen signal from O-*K* edge X-ray
256 absorption spectroscopy (XAS)³³. As a result, resonant inelastic X-ray scattering
257 (RIXS, probing depth: ~150 nm), with extra resolution along the emission energy
258 dimension, was selected as the tool-of-choice to clarify the role of oxygen³⁴.

259

260 O-K edge RIXS maps for Bare-LCO and TMA-LCO charged to 4.6 V are shown in
261 Figs. 5a and 5b, respectively, and the corresponding RIXS maps for pristine materials
262 are shown in Supplementary Fig. 12. Upon deep delithiation, the most obvious change
263 for Bare-LCO is the appearance of a well-distinguished isolated feature at an incident
264 energy of 531 eV (Fig. 5a), indicating the oxidization of O^{2-} to a higher valence state³⁵.
265 This RIXS feature becomes much weaker in TMA-LCO, indicating less participation
266 of oxygen redox in the outer shell of TMA-LCO particles (in view of the probing
267 depth of ~150 nm) compared with Bare-LCO, and the improved oxygen stability will
268 also contribute to the enhanced safety behaviours at high voltage (Supplementary Figs.
269 13-14). Moreover, the RIXS spectra demonstrate the superior stability of TMA-LCO
270 after 20 cycles compared with Bare-LCO, as shown in Fig. 5c. The elemental doping
271 likely changes the intrinsic electronic structure and consequently affects the redox
272 reactions, particularly the oxygen redox chemistry.

273

274 The route of surface reactions with electrolyte may also be affected due to the
275 different chemical reactivity of surface oxygen between Bare-LCO and TMA-LCO.
276 Both XPS and sXAS results confirm the distinct cathode/electrolyte interphase (CEI)
277 formed on Bare-LCO and TMA-LCO. As can be seen from the fitted O 1s XPS
278 spectra in Fig. 5d, lattice oxygen (shaded area) demonstrates a sharper peak that
279 overwhelms signals from the CEI components in TMA-LCO compared with
280 Bare-LCO, implying a relatively thinner and more stable CEI layer on TMA-LCO as

281 schematically illustrated in Fig. 5e. Such an interpretation is also supported by
282 quantitative analysis of XPS results as shown in Supplementary Figs. 15 and 16 and
283 Supplementary Table 7. Meanwhile, sXAS data collected in total electron yield (TEY)
284 and total fluorescence yield (TFY) modes can provide further contrast between
285 surface and bulk regions. Surface-sensitive TEY and bulk-sensitive TFY signals of
286 TMA-LCO and Bare-LCO in different cycle states are displayed as solid and dotted
287 lines, respectively, in Supplementary Fig. 17. Note that the TEY spectra do not simply
288 reproduce the TFY spectra, which can be attributed to interfacial reactions between
289 the electrode and the electrolyte. The relatively low pre-edge shoulder in TEY
290 indicates the decrease of high valence Co at the particle surface, particularly for
291 TMA-LCO. This phenomenon implies that different types of CEI layer form on
292 TMA-LCO and Bare-LCO, which is consistent with the O 1s XPS results. The stable
293 interface layer between cathode materials and electrolyte can also suppress Co
294 dissolution process (Supplementary Figs. 18-20). Therefore, the thinner and more
295 stable CEI layer is expected to contribute to the superior electrochemical
296 performances of TMA-LCO.

297

298 **DFT calculations and doping mechanism**

299 As Ti is rich on surface of TMA-LCO, first principles calculations were conducted
300 to gain fundamental understandings of the Ti surface doping mechanism in LiCoO₂.
301 In order to verify the experimental observations on Ti-distribution, the optimised
302 LiCoO₂ (104) slab model was used (Fig. 6a). We first considered replacing one Co

303 atom from different layers of the slab with Ti atom and compared the total ground
304 state energies of Ti-doped LiCoO_2 at different atomic layers, as listed in
305 Supplementary Table 8. Ti atom prefers to stay at the surface layer rather than in the
306 inner layers, with a 0.7 eV lower total energy. Then, replacing two Co atoms at the
307 surface layer with two Ti atoms and consider the distribution of Ti atoms at the
308 surface region. The different distances between the nearest Ti atoms on the (104)
309 surface are shown in Supplementary Fig. 21 and the total energies are listed in
310 Supplementary Table 9. All results indicate the preference of Ti occupancy at the
311 surface region. The incorporation of Ti into the LiCoO_2 lattice alters the electronic
312 structure as well. Fig. 6b compares the $2p$ states of the O atoms at the LiCoO_2 (104)
313 surface. Unoccupied O $2p$ states can be observed for the surface O atoms for both
314 Ti-doped and undoped LiCoO_2 in the delithiated $\text{Li}_{0.29}\text{CoO}_2$ state. However, the
315 unoccupied states above the Fermi level are significantly suppressed after Ti doping,
316 indicating suppressed charge deficiency in the surface layer. Fig. 6c displays the
317 relaxed structure of delithiated $\text{Li}_{0.29}\text{CoO}_2$ together with the charge density of the
318 surface O atoms compared with lithiated LiCoO_2 . The charge density contour clearly
319 shows that a substantial charge deficiency for the O atoms in the surface layer. The O
320 atoms near the Ti atoms lose less charge compared with those far from the Ti atoms.
321 Fig. 6d shows the optimised atomic structure of Ti-doped $\text{Li}_{0.29}\text{CoO}_2$, where Ti atoms
322 tend to stay in the surface layer. Charge analysis shows that the surface O atoms
323 around Ti atoms hold more charge (less oxidized), implying that Ti doping helps to
324 resist the charge deficiency of the O atoms upon delithiation. This agrees well with

325 the aforementioned RIXS results.

326

327 **Conclusions**

328 In summary, by virtue of Ti-Mg-Al co-doping, the physical properties of LiCoO₂,
329 including bulk crystal structure, electronic structure, particle shape and microstructure,
330 are effectively modified. Each doping element plays a different role in modifying the
331 material properties from different aspects. More specifically, Mg and Al atoms have
332 been successfully doped into the LiCoO₂ lattice, altering the phase transition
333 behaviour in the de/lithiation process. Mg doping can also increase the electronic
334 conductivity of the material. In contrast, even trace amount of Ti cannot be
335 completely incorporated into the LiCoO₂ lattice. The segregation of Ti at grain
336 boundaries and on surface, on one hand, modifies the microstructure of the sample
337 particle that is favourable for overall lithium diffusion and uniform internal strain
338 distribution, and on the other hand, inhibits the oxygen activity and stabilizes the
339 surface at high charging voltage. All of these effects synergistically add up to the
340 remarkably improved electrochemical performances.

341

342 It can be inferred from this work that the rational design of electrode materials
343 relies on comprehensive modifications from various aspects. Multi-scale and
344 multi-faceted characterisations are the key to gain insights into the roles of the
345 modification elements as well as the fundamental principles of the modification
346 approaches. Moreover, as verified in this specific case, the low solubility of Ti and,

347 thus, the segregation at the particle surface and grain boundaries plays a vital role in
348 electrochemical performances enhancement. The specific behaviour of Ti, which is
349 beyond the conventional doping scenario, implies the necessity to revisit elements
350 with a non-optimal solubility as dopants for material design and optimisation. This
351 would have profound implications for the design of electrode materials, well beyond
352 the present case of high voltage LiCoO₂ cathode for LIBs. Finally, it should be
353 pointed out that, from the perspective of practical applications, the performances of
354 LiCoO₂ at 4.6 V is still far from satisfactory. The development of high energy density
355 LIBs with high voltage LiCoO₂ requires comprehensive consideration of cathode,
356 anode, electrolyte and other key components, which calls for more research efforts
357 and engineering considerations. Nonetheless, this work unfolds the promising future
358 of dragging LiCoO₂ to even higher voltage and approaching the theoretical capacity
359 limit for practical applications.

360

361 **Methods**

362 **Material synthesis.** The LiCoO₂ materials were prepared by a solid-state reaction
363 method using Li₂CO₃ (99%), Co₃O₄ (99.7%), Al₂O₃ (99.9%), MgO (99%) and TiO₂
364 (99.9%) as precursors. All of the raw materials are industrial materials with battery
365 grade. An excess of 5 wt% Li₂CO₃ was used to compensate for the lithium loss during
366 high temperature synthesis. The starting materials were ground in an agate mortar and
367 the mixed powders were sintered at 1000 °C for 10 h in an alumina crucible to form
368 the intermediate products. Then the intermediate products were ground again in an

369 agate mortar and sintered for the second time at 900 °C for 10 h to get the final
370 products.

371 **XRD and SEM characterisation.** The XRD measurements were conducted by using
372 a Bruker D8 Advance diffractometer with Cu-K α radiation ($\lambda = 1.5405 \text{ \AA}$) in the scan
373 range (2θ) of 10° - 80° . For the *in situ* XRD experiments, a specially designed
374 Swagelok cell equipped with an X-ray-transparent aluminum window was used for
375 the *in situ* measurements. The *in situ* XRD patterns were collected with an interval of
376 40 min for each 2θ scan from 10° to 60° on charging and discharging at a current rate
377 of 0.1C (1C = 274 mA g^{-1}). The morphologies of the samples were investigated by a
378 scanning electron microscopy (SEM, Hitachi-S4800).

379 **XPS characterisation.** The X-ray photoelectron spectroscopy (XPS) were recorded
380 with a spectrometer having Mg/Al K α radiation (ESCALAB 250 Xi, ThermoFisher).
381 All binding energies were calibrated using the C 1s peak of the Super P at 284.4 eV as
382 an internal standard. In order to prevent the air exposure, all samples were transferred
383 by using a transfer box provided by ThermoFisher.

384 **TEM characterisation.** The TEM/STEM images, EDS, and EELS measurements
385 were performed by using a JEOL ARM200F microscope operating at 200 kV, which is
386 equipped with a probe-forming aberration corrector and Gatan image filter (GIF
387 Quantum 965).

388 **Half-cell assembly.** The LiCoO $_2$ /Li half-cell tests were conducted using coin cells
389 (CR2032), assembled in an argon filled glove-box. The working electrodes were
390 prepared by coating the mixture slurry of active material (80 wt%), super P (10 wt%)

391 and poly-vinylidene fluoride (PVDF, 10 wt%) on aluminum current collector,
392 followed by drying at 120 °C in vacuum for 10 h. The loading of active material was
393 controlled to between 3.0-4.0 mg cm⁻². The electrolyte was a solution of 1 M LiPF₆ in
394 ethylene (EC) and dimethyl carbonate (DMC) (1 :1 in volume). Lithium foil was used
395 as the counter electrode and Al₂O₃ coated polyethylene (PE) film was used as the
396 separator.

397 **Full-cell assembly.** The LiCoO₂/Graphite full-cell tests were conducted using stacked
398 pouch cells, assembled in a dry room. The cathode electrodes were prepared by
399 coating the mixture slurry of active material (95 wt%), carbon black (3 wt%) and
400 poly-vinylidene fluoride (PVDF, 2 wt%) on aluminum current collector, followed by
401 drying at 120 °C in vacuum for 10 h. The areal capacity was controlled to between
402 3.5-3.8 mAh cm⁻². The anode electrodes are composed of graphite (94.5 wt%), carbon
403 black (2 wt%), carboxy methyl cellulose sodium (CMC-Na, 1.5 wt%) and styrene
404 butadiene rubber (SBR, 2 wt%), fabricated following the same coating and drying
405 procedures. The capacity ratio between negative electrode and positive electrode (N/P)
406 was controlled to between 1.05-1.08. The electrolyte and separator were the same as
407 those used in half-cells.

408 **Electrochemical measurements.** The charge and discharge tests were carried out
409 using a Land CT2001A battery test system (Wuhan, PR China) in a voltage range of
410 3.0-4.6 V at various C-rates at room temperature for half-cells. For the full-cell tests, a
411 constant current and constant voltage (CCCV) mode was used. The cells were charged
412 at 0.33C to 4.55 V and then held until the current drops to 0.1C. The discharge

413 process was conducted at constant current mode at 0.33C. The full-cells were cycled
414 at the first two cycles for the formation process. For the first cycle, the pouch cells
415 were charged at 0.02C for 2 h. After resting for 5 minutes, the cells were charged at
416 0.2C to 4.55 V and then held at the voltage until the current dropped to 0.02C
417 (constant voltage process). Then, the cells were discharged at 0.2C to 3 V and rest for
418 5 minutes. For the second cycle, the cells were charged at 0.2C to 3.85 V and rest at
419 45 °C for 48 h to complete the formation process.

420 **Synchrotron 2D/3D fluorescence measurement and data analysis.** Nano and
421 micro fluorescence mapping was performed, respectively, at the Hard X-ray
422 Nano-probe (HXN) Beamline of the National Synchrotron Light Source II at
423 Brookhaven National Laboratory (NSLS-II, BNL) and the Beamline 2-3 of Stanford
424 Synchrotron Radiation Lightsource at SLAC National Accelerator Laboratory (SSRL,
425 SLAC). The nano probe experiment was carried out at 9.6 keV by focusing the
426 coherent monochromatic X-rays down to a 50 nm spot size using a Fresnel X-ray
427 zone plate. Tomography measurement was performed by collecting a total of 51
428 projections from -75° to 75° with 3° intervals. The tomographic reconstruction was
429 carried out using an iterative algorithm known as algebraic reconstruction technique
430 (ART). Further visualization and quantification of the imaging data were carried out
431 using a commercial software package, Avizo. The segmentation of sub-domains in the
432 imaged particle is based on the concentration ratio between the Co and Ti. As
433 discussed in the main text, the regions rich in Ti form interconnected networks (Figs.
434 4c and 4f) that divide the particle into 50 sub-domains (Fig. 4g). Micro probe

435 experiment was carried out using an K-B mirror focused X-ray spot of $\sim 1 \mu\text{m}$ to
436 image a large field of view covering many particles to ensure the statistical
437 representativeness (Supplementary Figure 11). The correlation analysis of Ti and Co
438 distribution is coupled with principle component analysis to separate the Ti-rich
439 domains from the area of the nominal composition.

440 **Synchrotron soft X-ray spectroscopy.** Soft X-ray spectroscopy measurements were
441 performed at beamline 8.0.1 of the Advanced Light Source at Lawrence Berkeley
442 National Laboratory (ALS, LBNL). The beamline is equipped with a spherical grating
443 monochromator which supplies linearly polarized soft X-ray with resolving power up
444 to 6000. The XAS spectra were collected in both TEY and TFY modes simultaneously.
445 TEY is surface sensitive with probing depth of $\sim 10 \text{ nm}$, while TFY provides bulk
446 information with probing depth of $\sim 150 \text{ nm}$. The energy of the O-K edge XAS spectra
447 were aligned based on O-K edge of Fe_2O_3 reference. The spectra intensities were
448 normalized to the beam flux measured by a gold mesh at upstream. The RIXS
449 experiments were carried out with the (high-resolution RIXS) hr-RIXS system at
450 beamline 8.0.1 in ALS. The newly build up system is equipped with a refocusing
451 mirror, a spherical pre-mirror, a variable line spacing grating and a high resolution X-
452 ray photon detector with entrance slitless design. The slitless operation improves the
453 acceptance angle of the spectrograph and increases the throughput without comprising
454 energy resolution. The incident excitation energy scale was calibrated according to
455 XAS of Fe_2O_3 reference sample, while subsequent emission energy was calibrated
456 using the elastically scattering line. The final data sets were presented in a

457 two-dimensional map, where the emission intensity was color coded as a function of
458 the incident excitation (ordinate) energy and emission energy (abscissa).

459 **First principles calculations.** All density functional theory (DFT) calculations were
460 performed with the Vienna ab initio simulation package (VASP)³⁶. The spin-polarized
461 generalized gradient approximation (GGA) with PBE function³⁷ was used to treat the
462 electron exchange-correlation interactions, and the projector-augmented wave (PAW)
463 approach³⁸ was used to take into account of the electron-ion interactions. Because
464 GGA cannot reproduce correctly the localized electronic states of the transition metal
465 oxide materials, GGA+U method was used^{39,40}. The U values for the Co-3*d* and Ti-3*d*
466 states were chosen to be 4.91 and 5.0 eV respectively^{41,42}. Furthermore, we included
467 the Van der Waals interaction throughout the calculations. A plane-wave basis with a
468 kinetic energy cutoff of 520 eV was used. The Monkhorst-Pack scheme⁴³ with $2 \times 3 \times$
469 1 k-point mesh was used for the integration in the irreducible Brillouin zone. The
470 lattice parameters and the ionic position were fully relaxed, and the final forces on all
471 atoms are less than 0.01 eV Å⁻¹. The calculation of the density of states (DOS) was
472 smeared by the Gaussian smearing method with a smearing width of 0.05 eV. The
473 LiCoO₂ (104) surface was simulated by symmetric periodic slab model containing 42
474 Li atoms, 84 O atoms and 42 Co atoms, with consecutive slabs separated by a 18 Å
475 vacuum layer. The delithiated state Li_{0.29}CoO₂ was modeled by extract 30 out of 42 Li
476 ions from the LiCoO₂ slab system. The Ti-doped LiCoO₂/Li_{0.29}CoO₂ slab system was
477 modeled by substituting one out of 42 Co ions by a Ti ion.

478

479 **Data Availability**

480 The data that support the plots within this paper and other finding of this study are
481 available from the corresponding author upon reasonable request.

482

483 **Acknowledgements**

484 The work was supported by funding from National Key R&D Program of China
485 (grant no. 2016YFB0100100), National Natural Science Foundation of China (grant
486 no. 51822211, 11574281) and the Foundation for Innovative Research Groups of the
487 National Natural Science Foundation of China (grant no. 51421002). The work done
488 at BNL were supported by the Assistant Secretary for Energy Efficiency and
489 Renewable Energy, Vehicle Technology Office of the U.S. Department of Energy
490 through the BMR Program, including Battery 500 Consortium under contract
491 DE-SC0012704. Use of the National Synchrotron Light Source II is supported by the
492 U.S. Department of Energy, an Office of Science user Facility operated by
493 Brookhaven National Laboratory under Contract No. DE-SC0012704. SLAC National
494 Accelerator Laboratory, is supported by the U.S. Department of Energy, Office of
495 Science, Office of Basic Energy Sciences under Contract No. DE-AC02-76SF00515.
496 Use of the Stanford Synchrotron Radiation Lightsource, SLAC National Accelerator
497 Laboratory, is supported by the U.S. Department of Energy, Office of Science, Office
498 of Basic Energy Sciences under Contract No. DE-AC02-76SF00515. Soft X-ray
499 spectroscopic data were collected at beamline 8.0.1 of the Advanced Light Source,
500 which is supported by the Director, Office of Science, Office of Basic Energy

501 Sciences, of the U.S. Department of Energy under Contract No.
502 DE-AC02-05CH11231. We gratefully acknowledge the help from beamline BL14W1
503 and BL08U at Shanghai Synchrotron Radiation Facility (SSRF, China).

504

505 **Author's contribution**

506 X.Y. and H.L. conceived the idea; J.N.Z. synthesized the materials and performed
507 electrochemistry measurements and X-ray diffraction measurements; C.M. performed
508 TEM measurements and analysis; Y.L., M.G., X.H., S.L. and Y.C. performed TXM
509 measurement and data analysis; Q.L. and W.Y. performed the soft X-ray spectroscopy
510 experiment and data analysis; O.C. and R.X. performed DFT analysis; Q.L., X.Y.,
511 J.N.Z., Y.L. and O.C. wrote the paper with critical inputs from all other authors; X.Y.,
512 Y.L. and H.L. edited and finalized the manuscript.

513

514 **Competing interests**

515 The authors declare no competing interests.

516

517 **References:**

- 518 1. Whittingham, M. S. Ultimate limits to intercalation reactions for lithium batteries. *Chem. Rev.*
519 **114**, 11414-11443 (2014).
520
- 521 2. Goodenough, J. B. Evolution of strategies for modern rechargeable batteries. *Accounts Chem.*
522 *Res.* **46**, 1053-1061 (2013).
523
- 524 3. Nitta N., Wu F., Lee J. T. & Yushin G. Li-ion battery materials: present and future. *Mater. Today*
525 **18**, 252-264 (2015).
526
- 527 4. Lin F.*et al.* Metal segregation in hierarchically structured cathode materials for high-energy

- 528 lithium batteries. *Nat. Energy*. **1**, 15004 (2016).
529
- 530 5. Lin F. *et al.* Surface reconstruction and chemical evolution of stoichiometric layered cathode
531 materials for lithium-ion batteries. *Nat. Commun.* **5**, 3529 (2014).
532
- 533 6. Liu C. F., Neale Z. G. & Cao G. Z. Understanding electrochemical potentials of cathode
534 materials in rechargeable batteries. *Mater. Today* **19**, 109-123 (2016).
535
- 536 7. Wang D. W. *et al.* Synthetic control of kinetic reaction pathway and cationic ordering in
537 high-Ni layered oxide cathodes. *Adv. Mater.* **29**, 1606715 (2017).
538
- 539 8. Radin M. D. *et al.* Narrowing the gap between theoretical and practical capacities in Li-ion
540 layered oxide cathode materials. *Adv. Energy Mater.* **7**, 1602888 (2017).
541
- 542 9. Kalluri S. *et al.* Surface engineering strategies of layered LiCoO₂ cathode material to realize
543 high-energy and high-voltage Li-ion cells. *Adv. Energy Mater.* **7**, 1601507 (2017).
544
- 545 10. Run Gu. *et al.* Improved electrochemical performances of LiCoO₂ at elevated voltage and
546 temperature with an in situ formed spinel coating layer. *ACS Appl. Mater. Inter.* **10**,
547 31271–31279 (2018).
548
- 549 11. Yano A., Shikano M., Ueda A., Sakaebe H. & Ogumi Z. LiCoO₂ degradation behavior in the
550 high-voltage phase transition region and improved reversibility with surface coating. *J.*
551 *Electrochem. Soc.* **164**, A6116-A6122 (2017).
552
- 553 12. Xu Y. H. *et al.* In situ visualization of state-of-charge heterogeneity within a LiCoO₂ particle
554 that evolves upon cycling at different rates. *ACS Energy Lett.* **2**, 1240-1245 (2017).
555
- 556 13. MacNeil D. D. & Dahn J. R. The reactions of Li_{0.5}CoO₂ with nonaqueous solvents at elevated
557 temperatures. *J. Electrochem. Soc.* **149**, A912-A919 (2002).
558
- 559 14. Doh C-H. *et al.* Thermal and electrochemical behaviour of C/Li_xCoO₂ cell during safety test. *J.*
560 *Power Sources* **175**, 881-885 (2008).
561
- 562 15. Whittingham M. S. Lithium batteries and cathode materials. *Chem. Rev.* **104**, 4271-4301
563 (2004).
564
- 565 16. Liu Q. *et al.* Approaching the capacity limit of lithium cobalt oxide in lithium ion batteries via
566 lanthanum and aluminium doping. *Nat. Energy* **3**, 936-943 (2018).
567
- 568 17. Lu Y-C., Mansour A. N., Yabuuchi N. & Shao-Horn Y. Probing the origin of enhanced stability of
569 “AlPO₄” nanoparticle coated LiCoO₂ during cycling to high voltages: combined XRD and XPS
570 studies. *Chem. Mater.* **21**, 4408-4424 (2009).
571

- 572 18. Kalluri S. *et al.* Feasibility of cathode surface coating technology for high-energy lithium-ion
573 and beyond-lithium-ion batteries. *Adv. Mater.* **29**, 1605807 (2017).
574
- 575 19. Wu N., Zhang Y., Wei Y., Liu H. & Wu H. Template-engaged synthesis of 1D hierarchical
576 chainlike LiCoO₂ cathode materials with enhanced high-voltage lithium storage capabilities.
577 *ACS Appl. Mater. Inter.* **8**, 25361-25368 (2016).
578
- 579 20. Wang F. *et al.* Stabilizing high voltage LiCoO₂ cathode in aqueous electrolyte with
580 interphase-forming additive. *Energ. Environ. Sci.* **9**, 3666-3673 (2016).
581
- 582 21. Wang J., Ji Y. J., Appathurai N., Zhou J. G. & Yang Y. Nanoscale chemical imaging of the
583 additive effects on the interfaces of high-voltage LiCoO₂ composite electrodes. *Chem.*
584 *Commun.* **53**, 8581-8584 (2017).
585
- 586 22. Wang L. L., Chen B. B., Ma J., Cui G. L. & Chen L. Q. Reviving lithium cobalt oxide-based
587 lithium secondary batteries-toward a higher energy density. *Chem. Soc. Rev.* **47**, 6505-6602
588 (2018).
589
- 590 23. Koyama Y., Arai H., Tanaka I., Uchimoto Y. & Ogumi Z. First principles study of dopant
591 solubility and defect chemistry in LiCoO₂. *J. Mater Chem. A* **2**, 11235-11245 (2014).
592
- 593 24. Gopukumar S., Jeong Y. & Kim K B. Synthesis and electrochemical performance of tetravalent
594 doped LiCoO₂ in lithium rechargeable cells. *Solid State Ionics* **159**, 223-232 (2003).
595
- 596 25. Tukamoto H. & West A. R. Electronic conductivity of LiCoO₂ and its enhancement by
597 magnesium doping. *J. Electrochem. Soc.* **144**, 3164-3168 (1997).
598
- 599 26. Zou M., Yoshio M., Gopukumar S. & Yamaki J. Synthesis of high-voltage (4.5 V) cycling doped
600 LiCoO₂ for use in lithium rechargeable cells. *Chem. Mater.* **15**, 4699-4702 (2003).
601
- 602 27. Kim S. *et al.* Self-assembly of core-shell structures driven by low doping limit of Ti in LiCoO₂:
603 first-principles thermodynamic and experimental investigation. *Phys. Chem. Chem. Phys.* **19**,
604 4104-4113 (2017).
605
- 606 28. Van der Ven A., Aydinol M. K., Ceder G., Kresse G. & Hafner J. First-principles investigation of
607 phase stability in Li_xCoO₂. *Phys. Rev. B* **58**, 2975-2987 (1998).
608
- 609 29. Amatucci G. G., Tarascon J. M. & Klein L. C. CoO₂, the end member of the Li_xCoO₂ solid
610 solution. *J. Electrochem. Soc.* **143**, 1114-1123 (1996).
611
- 612 30. Reimers J. N. & Dahn J. R. Electrochemical and In situ X-Ray diffraction studies of lithium
613 intercalation in Li_xCoO₂. *J. Electrochem. Soc.* **139**, 2091-2097 (1992).
614
- 615 31. Yang S-H., Levasseur S., Weill F. & Delmas C. Probing lithium and vacancy ordering in O3

616 layered Li_xCoO_2 ($x \approx 0.5$): an electron diffraction study. *J. Electrochem. Soc.* **150**, A366-A373
617 (2003).
618

619 32. Yang W. *et al.* Key electronic states in lithium battery materials probed by soft X-ray
620 spectroscopy. *J. Electron Spectrosc.* **190**, 64-74 (2013).
621

622 33. Yoon W-S. *et al.* Oxygen contribution on Li-Ion intercalation-deintercalation in LiCoO_2
623 investigated by O K-Edge and Co L-Edge X-ray absorption spectroscopy. *J. Phys. Chem. B* **106**,
624 2526-2532 (2002).
625

626 34. Kotani A. & Shin S. Resonant inelastic x-ray scattering spectra for electrons in solids. *Rev.*
627 *Mod. Phys.* **73**, 203-246 (2001).
628

629 35. Yang W. & Devereaux T. P. Anionic and cationic redox and interfaces in batteries: Advances
630 from soft X-ray absorption spectroscopy to resonant inelastic scattering. *J. Power Sources*
631 **389**, 188-197 (2018).
632

633 36. Kresse G. & Furthmüller J. Efficient iterative schemes for ab initio total-energy calculations
634 using a plane-wave basis set. *Phys. Rev. B* **54**, 11169-11186 (1996).
635

636 37. Perdew J. P., Burke K. & Ernzerhof M. Generalized gradient approximation made simple. *Phys.*
637 *Rev. Lett.* **77**, 3865-3868 (1996).
638

639 38. Kresse G. & Joubert D. From ultrasoft pseudopotentials to the projector augmented-wave
640 method. *Phys. Rev. B* **59**, 1758-1775 (1999).
641

642 39. Anisimov V. I., Zaanen J. & Andersen O. K. Band theory and Mott insulators: Hubbard U
643 instead of Stoner I. *Phys. Rev. B* **44**, 943-954 (1991).
644

645 40. Vladimir I. A., Aryasetiawan F. & Lichtenstein AI. First-principles calculations of the electronic
646 structure and spectra of strongly correlated systems: the LDA + U method. *J. Phys-Condens.*
647 *Mat.* **9**, 767 (1997).
648

649 41. Zhou F., Cococcioni M., Marianetti C. A., Morgan D. & Ceder G. First-principles prediction of
650 redox potentials in transition-metal compounds with LDA+U. *Phys. Rev. B.* **70**, 235121 (2004).
651

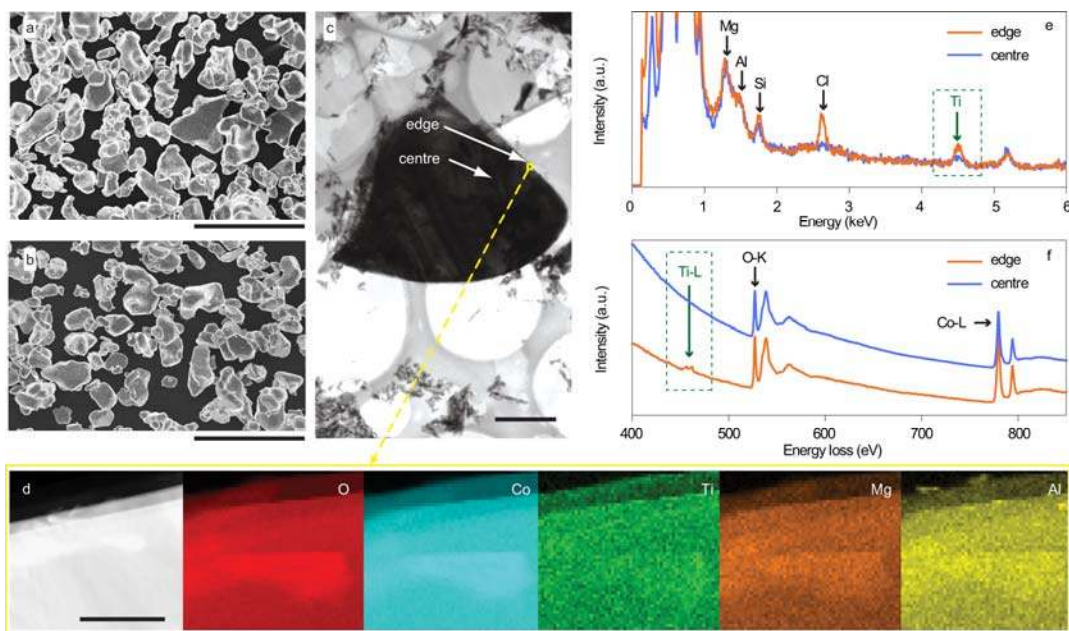
652 42. Tanaka S. *et al.* Atomic and electronic structures of $\text{Li}_4\text{Ti}_5\text{O}_{12}/\text{Li}_7\text{Ti}_5\text{O}_{12}$ (001) interfaces by
653 first-principles calculations. *J. Mater. Sci.* **49**, 4032-4037 (2014).
654

655 43. Monkhorst H. J. & Pack J. D. Special points for Brillouin-zone integrations. *Phys. Rev. B* **13**,
656 5188-5192 (1976).
657

658

659 **Figures**

660



661

662 **Fig. 1 Morphology and elemental distribution in Bare-LCO and TMA-LCO.**

663 SEM images of (a) Bare-LCO and (b) TMA-LCO, scale bar: 20 μm . (c)

664 Cross-sectional TEM image of TMA-LCO, scale bar: 2 μm . (d) HADDF-STEM

665 image and EDS elemental mappings of O, Co, Ti, Mg, and Al (scale bar: 100 nm) of

666 the selected region indicated by the yellow rectangular in (c), demonstrating an

667 overall homogeneous distribution of the doping elements Ti, Mg and Al except for the

668 Ti-rich edge region (see the enlarged images and integrated intensity profiles in

669 Supplementary Fig. 5). (e) EDS and (f) EELS spectra collected separately from the

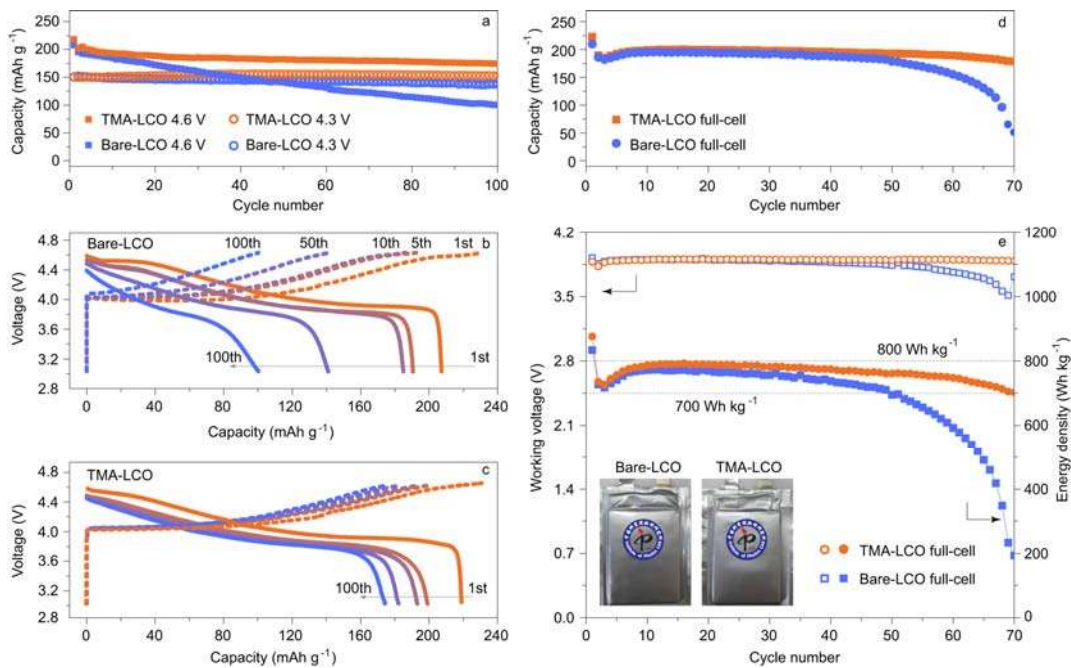
670 edge (surface) and centre (interior) regions of TMA-LCO, as indicated by the white

671 arrows in (c). The rectangular in green colour highlights the signal of Ti, revealing the

672 slightly increased concentration of Ti in the edge region by comparing with the centre

673 region in the TMA-LCO particle.

674



675

676 **Fig. 2 Electrochemical characterisation of Bare-LCO and TMA-LCO.** (a)

677 Comparison of cycle performances of LiCoO₂|Li half-cells with Bare-LCO and

678 TMA-LCO. Charge-discharge curves of (b) Bare-LCO and (c) TMA-LCO half-cells

679 for 1st, 5th, 10th, 50th and 100th cycles. The charge and discharge tests were

680 conducted at 0.1C for the 1st cycle and 0.5C for the subsequent cycles. (d) Cycle

681 performances of LiCoO₂|Graphite full-cells with Bare-LCO and TMA-LCO. A CCCV

682 mode was used for the full-cell tests. For the charge process, the cells were charged at

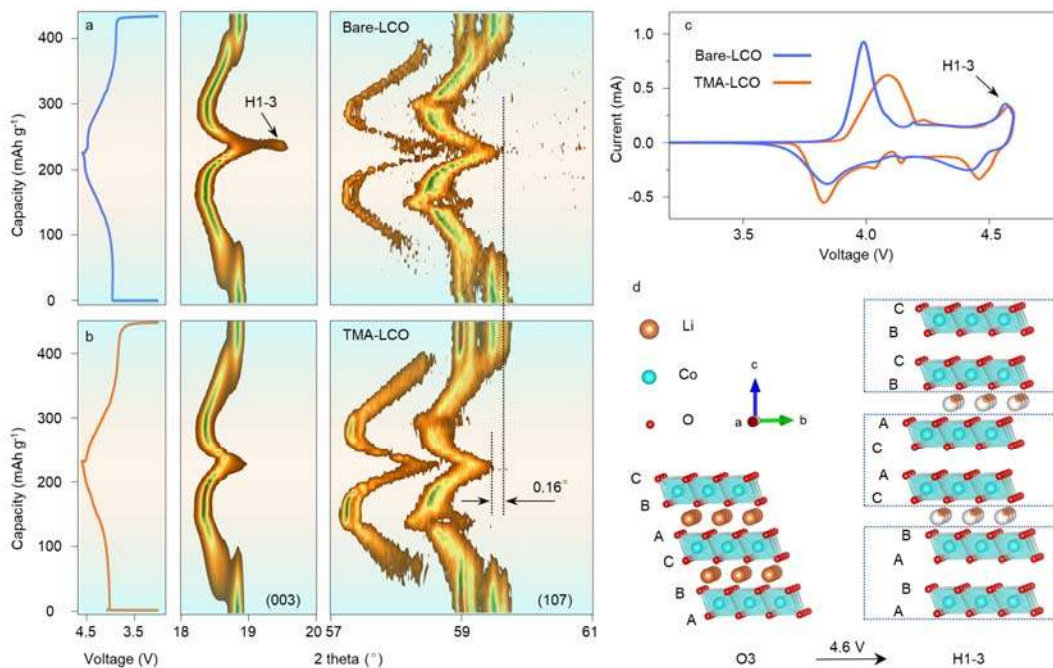
683 0.33C to 4.55 V and then held the voltage until the current dropped to 0.1C. The

684 discharge current was 0.33C. (e) The discharge voltage of the full-cells and energy

685 density of cathode materials as a function of cycle number. The inset shows the pouch

686 cells after 70th cycle and obvious gas generation can be observed in the

687 Bare-LCO|Graphite pouch cell.



688

689 **Fig. 3 Structural evolution during initial charge-discharge process.** *In situ* XRD

690 evolution of (a) Bare-LCO and (b) TMA-LCO at the (003) and (107) diffraction

691 peaks, with the corresponding charge-discharge curves aligned to the left. A

692 suppressed O3 to H1-3 phase transition with smaller (107) diffraction peak shift

693 (0.16°) can be observed in TMA-LCO at 4.6V charged state. (c) Cyclic voltammetry

694 results of Bare-LCO and TMA-LCO. (d) Schematic diagrams on atomic stacking of

695 Li_xCoO_2 in the O3 and H1-3 phases. For pristine LiCoO_2 , it can be described as O3

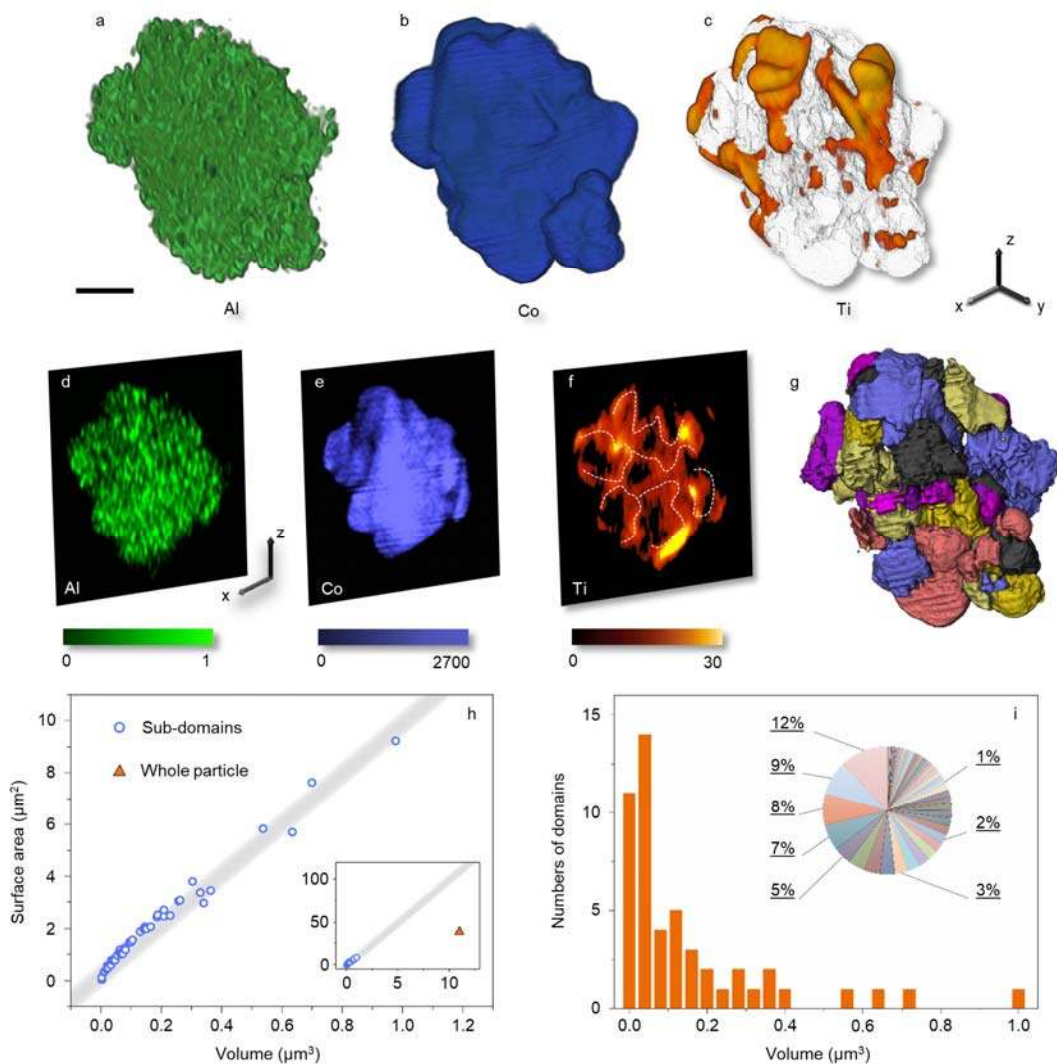
696 phase with oxygen layer stacking sequence of ABCABC. Upon charging to 4.6 V,

697 such sequence changes into ABABCACABCBC and the O3 to H1-3 phase transition

698 occurs.

699

700



701

702 **Fig. 4 3D X-ray tomography reconstruction and element distribution in**

703 **TMA-LCO.** 3D spatial distributions of (a) Al, (b) Co and (c) Ti probed by FY-STXM.

704 Elemental distributions of (d) Al, (e) Co and (f) Ti over the virtual x-z slice through

705 the centre of the particle. (g) Identified and visualised subdomain formation. Note that

706 different colours are used to distinguish adjacent subdomains. (h) Quantification of

707 the volume and the surface area of the sub-domains and the entire particle as a whole

708 (see inset for a zoom-out view). The grey shadow is the linear trend extracted from

709 the sub-domains' data. **(i)** The volume distribution of all the sub-domains. The inset
710 shows the volume fraction of each individual sub-domains, highlighting the existence
711 of a few large sub-domains, which make up nearly 50% of the total volume, and a
712 large number of small domains. The scale bar in **(a)** is 1 μm .

713

714

715

716

717

718

719

720

721

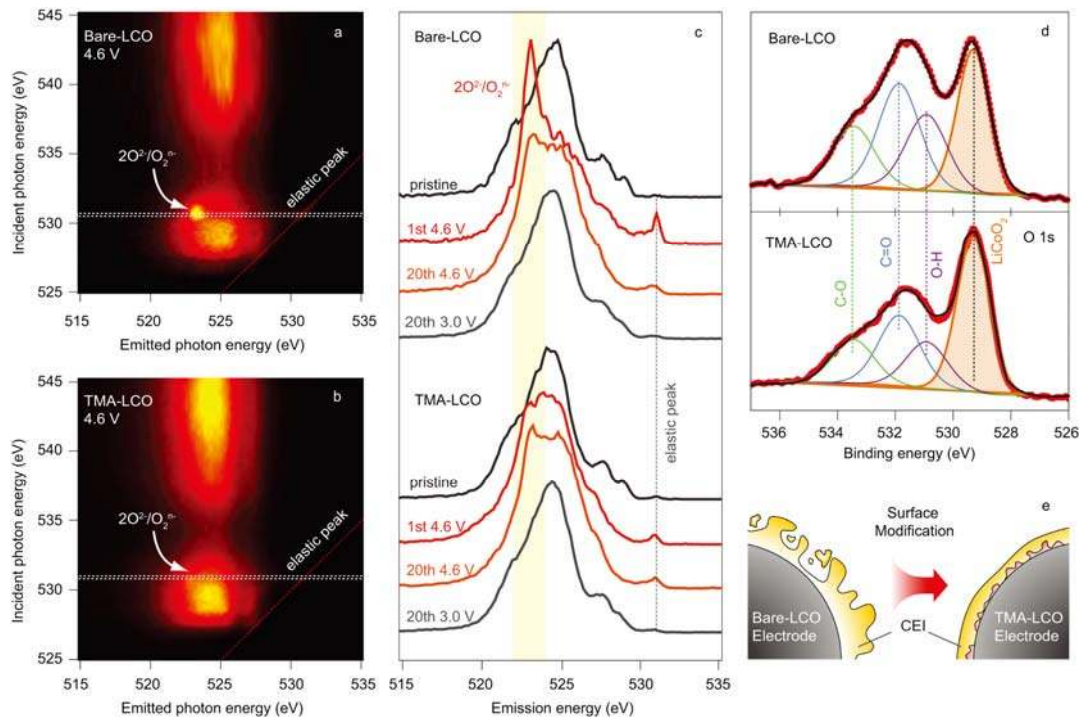
722

723

724

725

726



727

728 **Fig. 5 Revealing the surface chemistry by soft X-ray spectroscopy.** O-K edge

729 RIXS maps collected on 4.6 V charged (a) Bare-LCO and (b) TMA-LCO. With a low

730 X-ray irradiation energy of ~ 529 eV, O $1s$ electrons get excited into unoccupied Co

731 $3d-O 2p$ hybridisation states, whereas irradiation with high-energy X-rays (~ 540 eV)

732 excites O $1s$ electrons into Co $4sp-O 2p$ hybridisation states. (c) RIXS spectra

733 collected on Bare-LCO and TMA-LCO in pristine, 4.6 V charged states, and 3.0V

734 discharged state after the 20th cycles with an X-ray excitation energy of 531 eV. The

735 electrodes were prepared from cells cycled at a current rate of 0.1C. (d) O $1s$ XPS

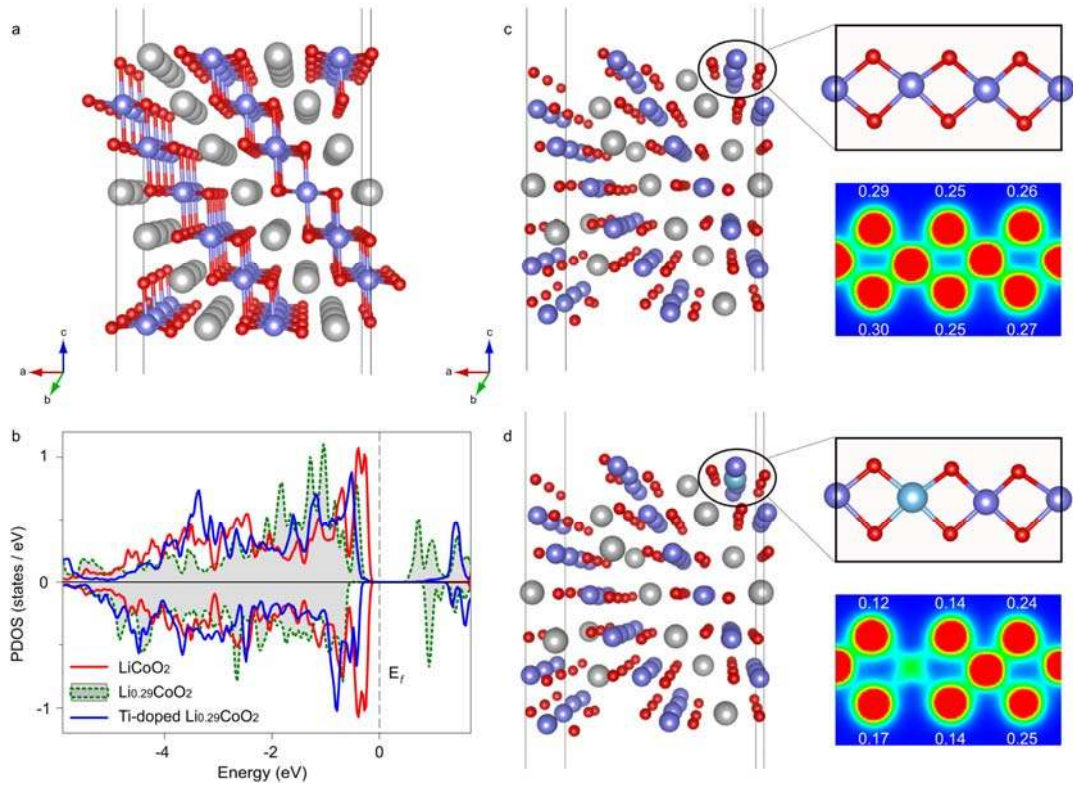
736 spectra of Bare-LCO (top) and TMA-LCO (bottom) electrodes after the 10th cycle at

737 3.0 V discharged state. (e) An illustration of the differences in CEI between

738 Bare-LCO and TMA-LCO.

739

740



741

742 **Fig. 6 DFT calculations for Ti substitution that can modify the surface**

743 **electronic structure. (a)** Optimised atomic structure of the (104) slab of LiCoO₂.

744 The grey, blue and red spheres represent Li, Co and O atoms, respectively. The

745 larger cyan sphere in (d) represents the Ti ion substituting the corresponding Co ion.

746 (b) Projected density of states of the surface O atom at the (104) surface of LiCoO₂,

747 Li_{0.29}CoO₂ and Ti-doped Li_{0.29}CoO₂. (c) Optimised atomic structure of the (104)

748 slab of Li_{0.29}CoO₂. (d) Optimised atomic structure of the Ti-doped (104) slab of

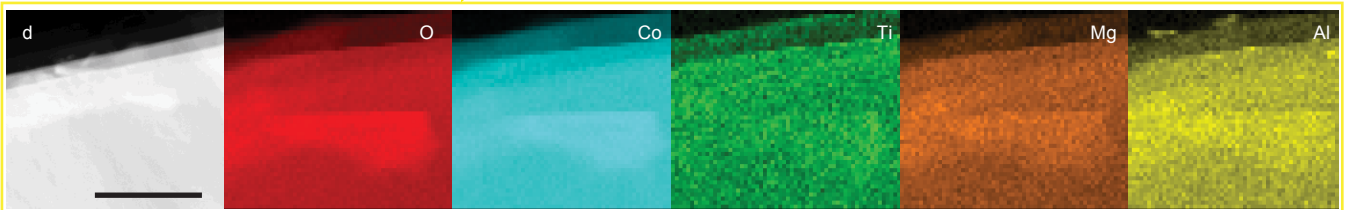
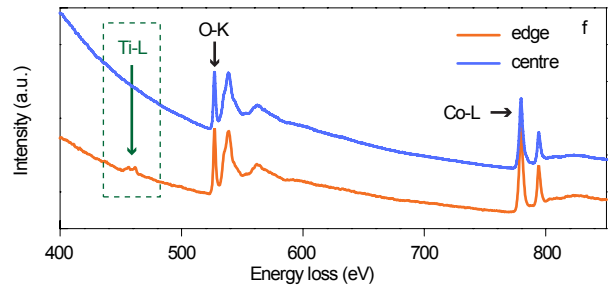
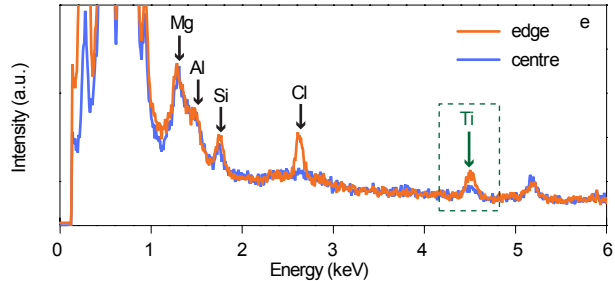
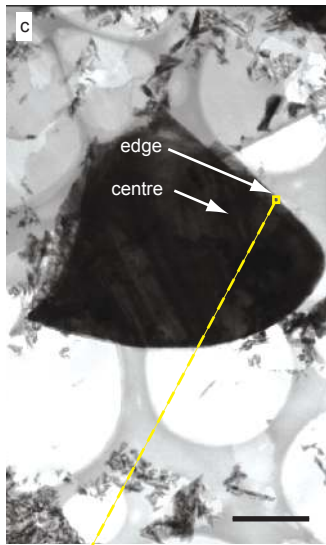
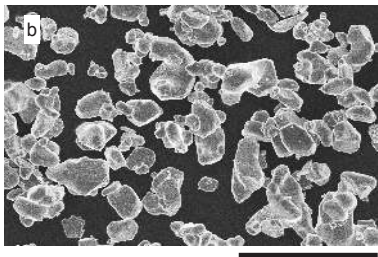
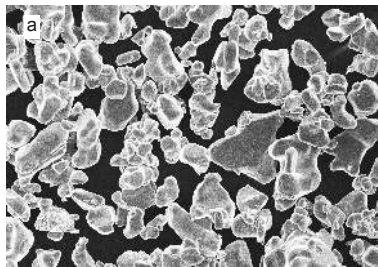
749 Li_{0.29}CoO₂. The insets on the right-hand side for (c) and (d) are the top views of the

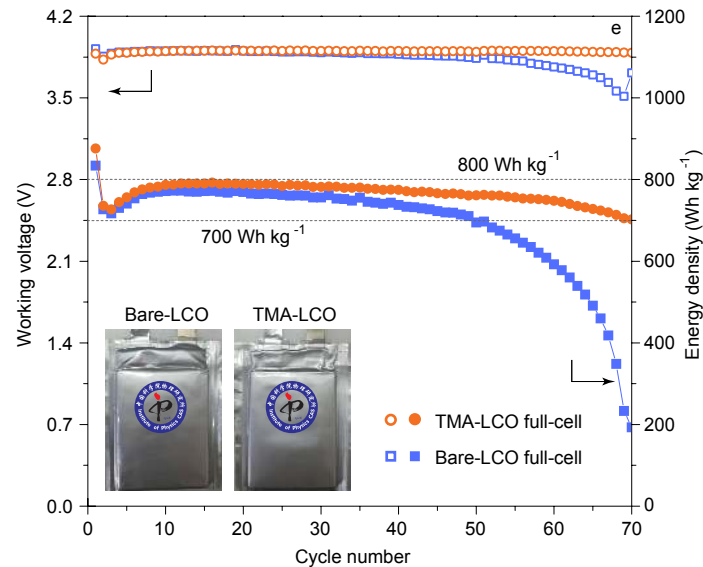
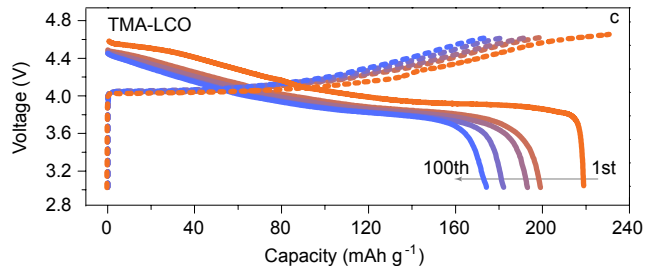
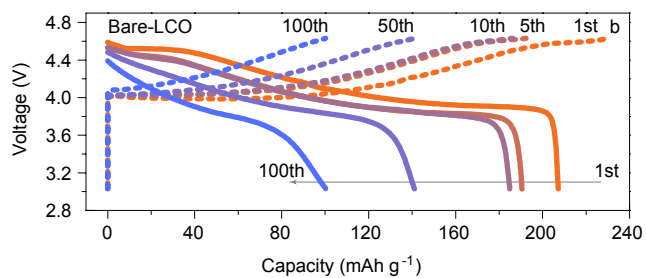
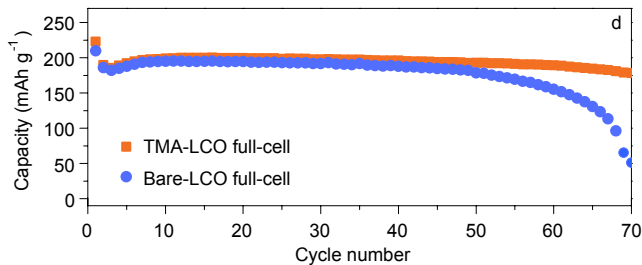
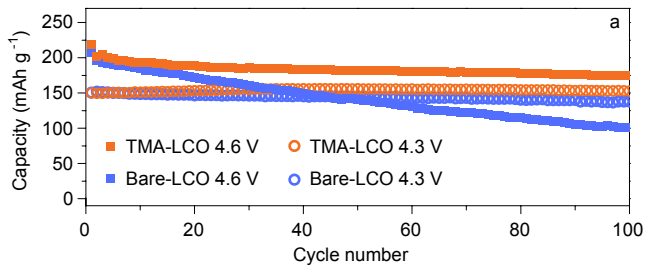
750 corresponding surface structures and the surface charge density contours,

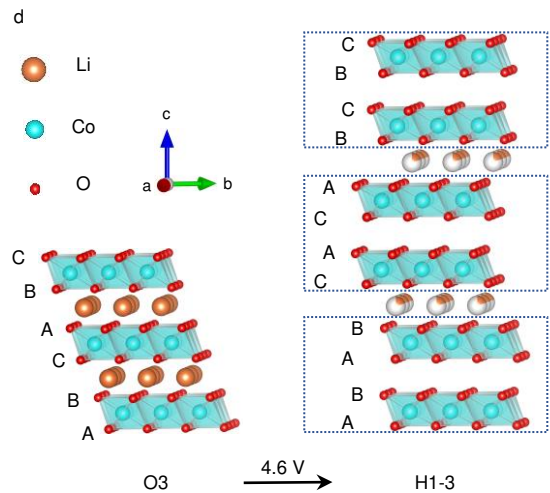
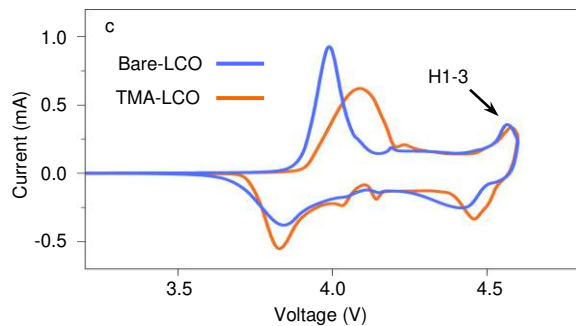
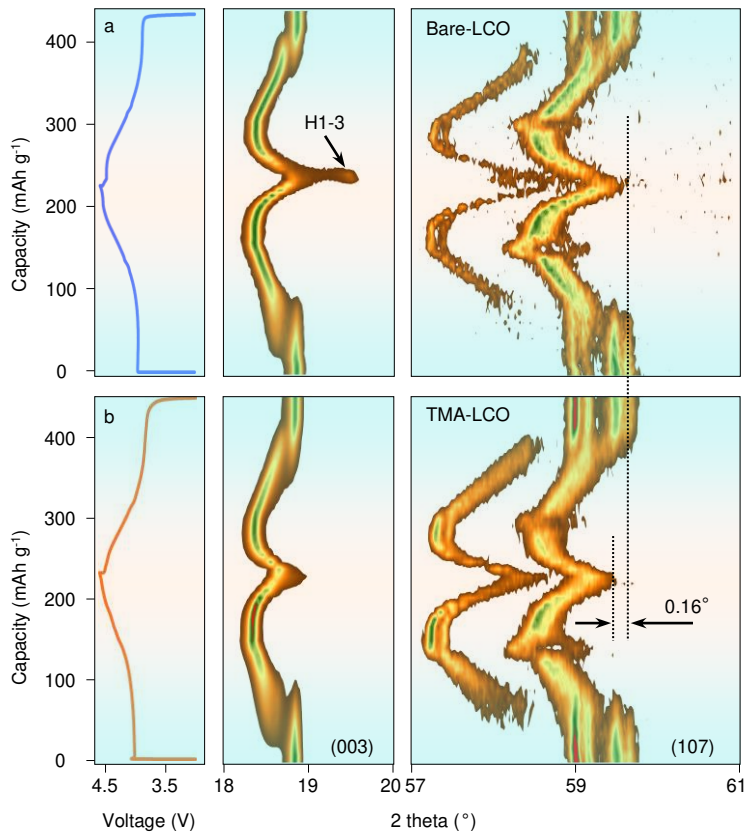
751 respectively. The numbers on the charge density contours are the charge loss (in

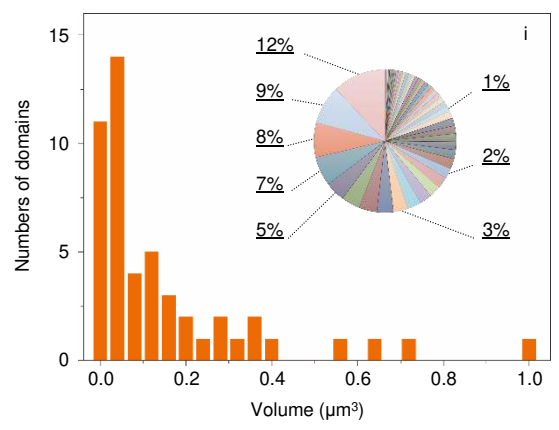
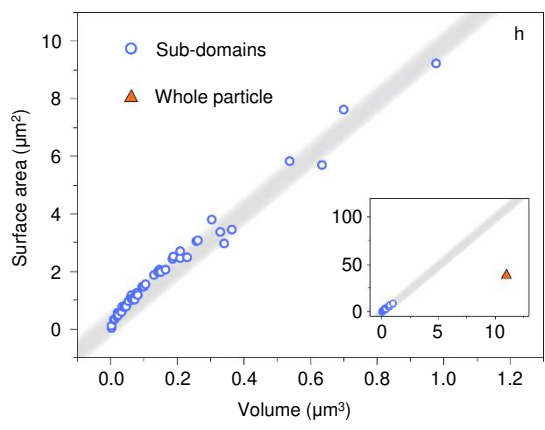
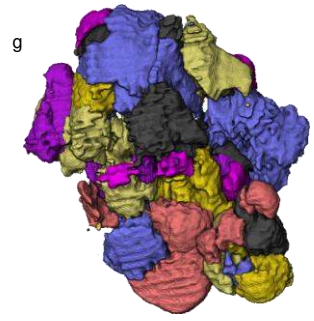
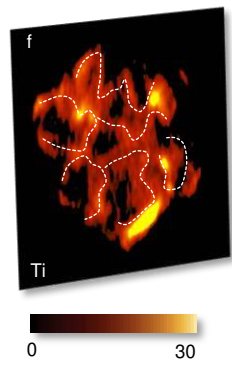
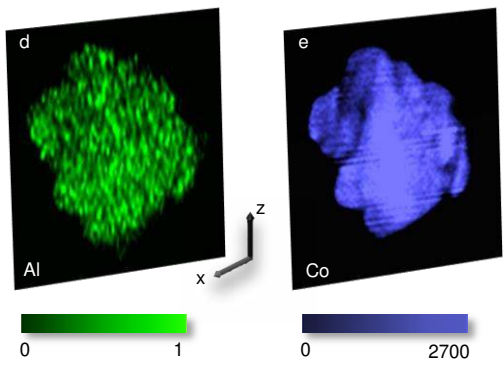
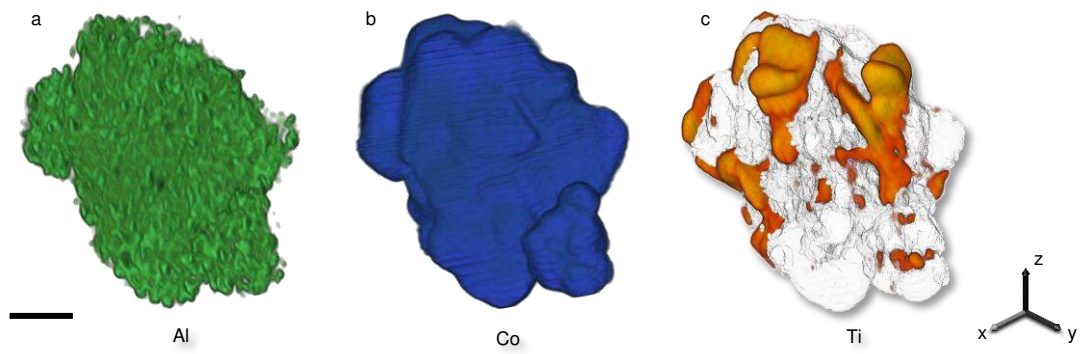
752 electron) of the corresponding O atom upon delithiation from LiCoO₂ to Li_{0.29}CoO₂

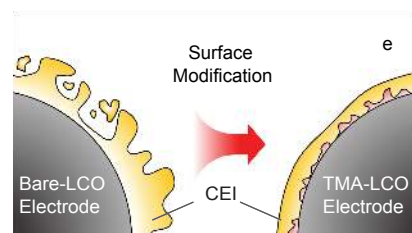
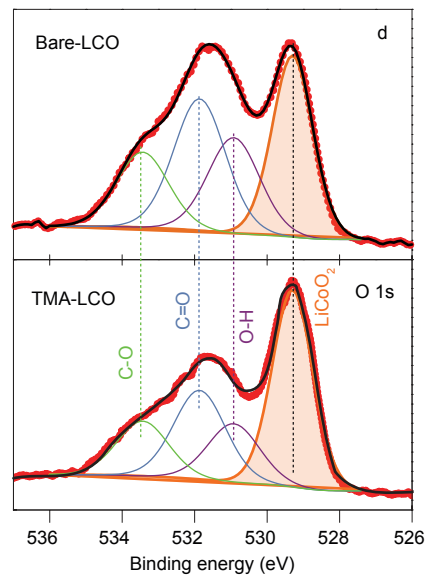
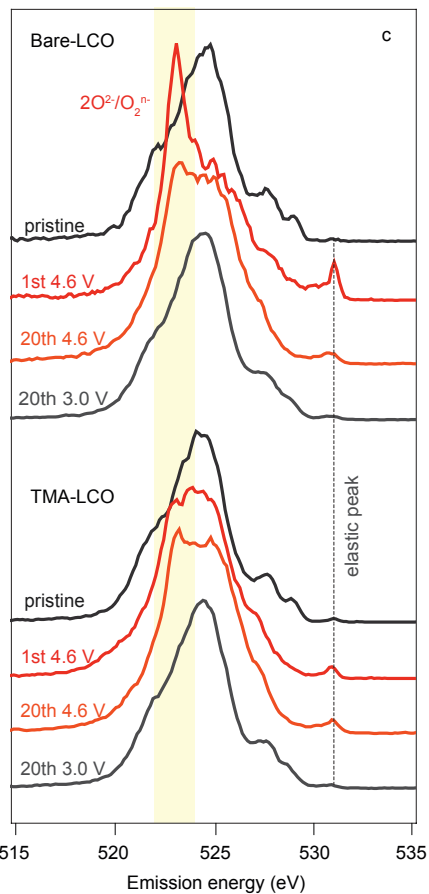
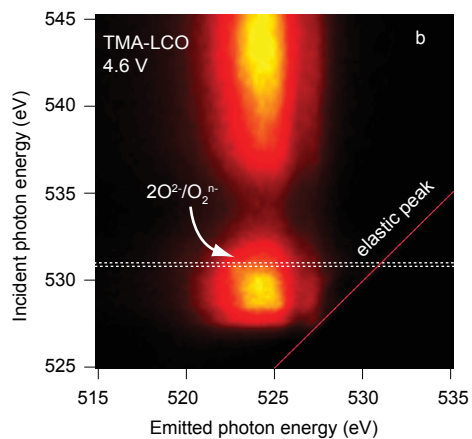
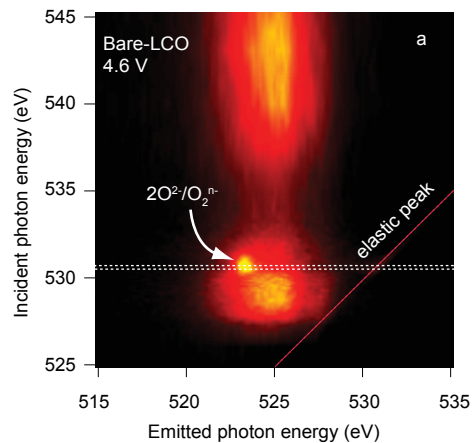
753 obtained from Bader charge analysis.



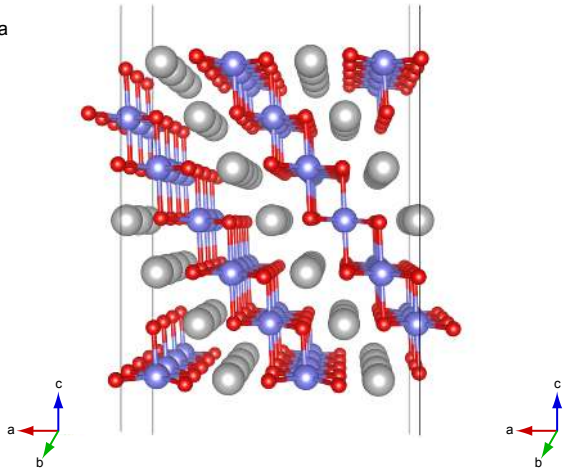




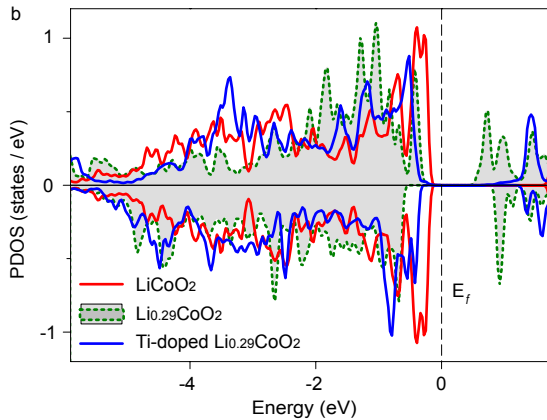




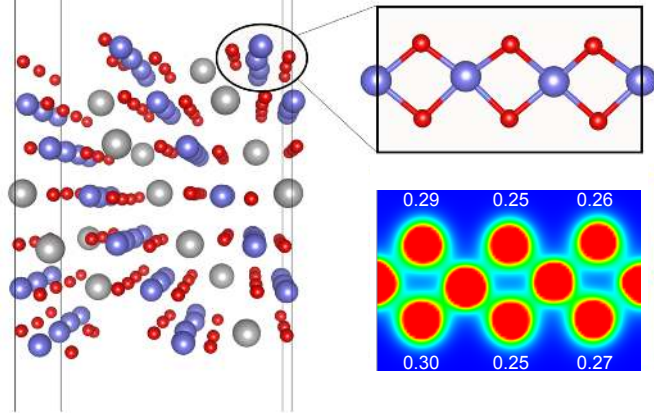
a



b



c



d

